metals

MDPI

Article

Investigation on the Microstructure and Mechanical Properties of Ni-Based Superalloy with Scandium

Lin Ye [1,2], Feng Liu [1,2], Heng Dong [1,2], Xiaoqiong Ouyang [1,2], Xiangyou Xiao [1,2], Liming Tan [1,2,3,*] and Lan Huang [1,2,*]

[1] State Key Laboratory of Powder Metallurgy, Central South University, Changsha 410083, China
[2] Research Institute of Powder Metallurgy, Central South University, Changsha 410083, China
[3] Foshan (Southern China) Institute for New Materials, Foshan 528200, China
* Correspondence: limingtan@csu.edu.cn (L.T.); lhuang@csu.edu.cn (L.H.)

Abstract: In this work, a method concerning thermal consolidation is proposed to simulate the traditional powder metallurgy process and accomplish the composition screening of powder metallurgy Ni-based superalloys U720Li and RR1000 with rare metal scandium, and superalloys with zero scandium addition, medium scandium addition and high scandium addition are selected. Then effects of scandium on the microstructure and mechanical properties of superalloys are further investigated through fast hot pressed sintering. The results indicate that scandium doping can effectively refine the grain through modifying the size and volume fraction of primary γ′ precipitates at the grain boundary. Meanwhile, scandium can promote the growth and precipitation of secondary γ′ precipitates to some extent. Due to the comprehensive effects of γ′ precipitate modification and grain boundary strengthening, as-sintered U720Li with 0.043 wt.% scandium presents an excellent combination of tensile strength and ductility at ambient and elevated temperature while as-sintered RR1000 with 0.064 wt.% scandium has a good performance at elevated temperature.

Keywords: Ni-based superalloy; scandium; grain; γ′ precipitate; tensile property

Citation: Ye, L.; Liu, F.; Dong, H.; Ouyang, X.; Xiao, X.; Tan, L.; Huang, L. Investigation on the Microstructure and Mechanical Properties of Ni-Based Superalloy with Scandium. *Metals* **2023**, *13*, 611. https://doi.org/10.3390/met13030611

Academic Editors: Andrzej Gontarz and Grzegorz Winiarski

Received: 27 February 2023
Revised: 15 March 2023
Accepted: 16 March 2023
Published: 18 March 2023

1. Introduction

As one of the key thermal components of aerospace engine, turbine disks with high quality and performance guarantee the reliability and safety of the aero-engine. Powder metallurgy (P/M) Ni-based superalloys have been widely used to manufacture high-performance aero-engine turbine disks due to their excellent fatigue life, rupture strength and creep resistance [1–3]. With the development of current areo-engine moving towards higher thrust-to-weight ratio and power-to-weight ratio, it has put forward higher requirements on the materials and fabricating process of turbine discs [4]. Nowadays, conventional P/M Ni-based superalloys have been widely applied, and some countries have begun to develop the new generation of P/M Ni-based superalloys with improved service temperature up to 800 °C [5].

The development of P/M Ni-based superalloys is based on the composition design. The representative of the high-strength P/M Ni-based superalloys like René95 and U720 have a higher content of Al, Ti and Nb, which facilitates the formation of gamma prime phase. As one of the most important precipitates in the Ni-based superalloy, gamma prime phase plays the leading role of strengthening through interactions with dislocations during plastic deformation. And the size [6], distribution, volume fraction of gamma prime phase are the main factors affecting the strength [7] and creep performance [8] of Ni-based superalloy. In contrast, the damage-tolerance P/M Ni-based superalloys like René88DT and U720Li have lowered the content of Al, Ti and Nb while the content of solid solution strengthening elements W and Mo are increased. Thereafter, Ta was added into the next-generation P/M Ni-based superalloys such as René104 and RR1000.

However, the composition design by means of adjusting several certain elements of the superalloy has stuck in a bottleneck, thus it is necessary to consider introducing new elements such as rare earth element [9]. It has been widely reported that rare earth element can significantly refine the grain of the superalloy by segregating at the grain boundaries and hindering the growth of the grain cell [10]. Meanwhile it can effectively optimize the precipitation phase of the superalloy [11]. With only a little addition, rare earth element can boost the tensile properties [12,13], rupture life [14] and oxidation resistance [15] of the superalloy. Among those rare earth elements, Y [16–19], La [20–22] and Ce [23–26] have widespread adoption in superalloys. In addition, Sc is reported to have similar benefits on the superalloy. Deng et al. [10] demonstrated that Sc had a good affinity to oxygen which could purify the grain boundary and reinforce tensile properties. Wei et al. [27,28] illustrated that Sc contributed to the refinement of grains, crack elimination and improvement of mechanical properties of the superalloy through additive manufacturing. However, the optimal addition of Sc in P/M superalloys remains to be investigated. On the other hand, as traditional powder metallurgy technology has long cycle, high cost and low fault tolerance.

In this work, a new method concerning thermal consolidation was proposed to simulate the traditional powder metallurgy process, and accelerate the composition screening and verification of two Sc-doped superalloy, U720Li and RR1000, which have a close gamma prime phase volume fraction. Then the microstructure and mechanical properties of U720Li and RR1000 with different addition of Sc were further studied through fast hot pressed sintering.

2. Materials & Methods

2.1. Materials

Vacuum induction melting (VIM) was adopted to prepare the master alloys of Sc-doped superalloy U720Li and RR1000 in the industrial conditions. Specifically, Sc element was introduced as pure metal and part of Al-Sc intermediate alloy during the melting process. Then the powder of two kinds of Sc-doped superalloy U720Li and RR1000 were prepared by vacuum induction argon atomization. The chemical composition of two kinds of Sc-doped superalloy powder are shown in Tables 1 and 2 respectively.

Table 1. Chemical composition of Sc-doped U720Li powder in wt.%.

Alloy	Ni	Cr	Co	Mo	W	Al	Ti	Zr	Sc
U-0	Bal.	16.1	14.3	3.23	1.53	1.86	4.38	0.025	0
U-0.027	Bal.	15.8	14.4	3.26	1.52	1.81	4.35	0.024	0.027
U-0.043	Bal.	15.9	14.3	3.23	1.5	1.8	4.34	0.021	0.043
U-0.066	Bal.	15.8	14	3.2	1.5	1.8	4.3	0.026	0.066

Table 2. Chemical composition of Sc-doped RR1000 powder in wt.%.

Alloy	Ni	Cr	Co	Mo	Ta	Al	Ti	Hf	Sc
R-0	Bal.	14.3	19.5	4.97	1.82	2.58	3.18	0.41	0
R-0.021	Bal.	14.5	19.8	4.98	1.79	2.55	3.24	0.42	0.021
R-0.048	Bal.	14.5	19.6	4.98	1.83	2.58	3.18	0.41	0.048
R-0.064	Bal.	14.4	19.5	4.97	1.84	2.6	3.19	0.45	0.064

2.2. Thermal Consolidation Process

The powder was packed in a cylindrical stainless-steel mold whose height and diameter are 15 mm and 10 mm respectively. Then the mold full of powder was welded by vacuum electron beam welding below 10^{-1} Pa. Thermal consolidation was conducted by Gleeble 3180D at the temperature of 1050 °C and 1150 °C with strain rate of 1 s^{-1} and 5 s^{-1}. Before the consolidation, tantalum sheets and graphite sheets were attached to the two ends of the mold with high temperature lubricant, which can reduce friction and make the consolidation deformation more even. Additionally, thermal-couple wires were

welded on the center of the mold surface in the height direction, which can monitor the temperature condition during the whole thermal consolidation process. Then the mold full of powder was heated through resistance heating to the setting temperature at the rate of 5 °C·s^{-1} and remaining for 3 min. Once the process of heating and heat preservation was completed, the consolidation was accomplished according to the procedure and the powder was compressed together with mold. Then the specimen was quenched in the water. All the specimens were compressed to an engineering strain of 80% with setting strain rate. The process of thermal consolidation is shown in Figure 1.

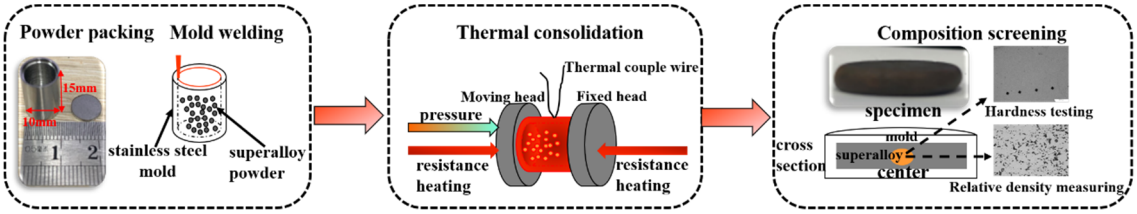

Figure 1. Schema of the thermal consolidation process.

2.3. Fast Hot Pressed Sintering Process

The alloy powder was packed into a graphite mold with a height of 70 mm and a diameter of 30 mm, and the powder was vibrated during the packing process. Subsequently, the mold full of powder was placed into the FHP-828 fast hot pressed sintering furnace and pre-pressed with a force of 40 MPa to compact the powder. Then fast hot pressed sintering was carried out below 10^{-1} Pa with a sintering temperature of 1150 °C and a holding time of 10 min, and the sintering pressure is 50 MPa.

2.4. Microstructure Characterization

The specimens prepared by thermal consolidation were observed through a LEICA DM4000M optical microscopy (OM), which were mechanically polished by abrasive papers and aluminum oxide of 50 nm in advance. The specimen density was calculated through ImageJ software by counting the total area of pores.

The specimens fabricated by fast hot pressed sintering were observed by a Quanta 650FEG scanning electron microscope (SEM) performed at 20 kV. The specimens for gamma prime phase observation were mechanically polished and etched in a solution of 100 mL HCl + 100 mL ethanol + 5 g $CuCl_2$. The size and volume fraction of gamma prime phase were quantitatively measured by ImageJ software. Energy dispersive spectroscopy (EDS) was also performed for semi-quantitative analysis of elements. Electron backscatter diffraction (EBSD) was employed with a voltage of 20 kV and a step size of 1 μm to measure the size of grains. The density of the specimens was determined by Archimedes method.

2.5. Mechanical Test

The microhardness test was carried out on the center of the specimens by a vickers hardness tester (THV-10) with a load of 3 kg and a dwell time of 10 s. The standard deviation was calculated based on 8 measurements.

A sub-solvus heat treatment was conducted to the RR1000 specimens, which consists of a solution heat treatment at 1120 °C for 4 h followed by air cooling and an aging heat treatment at 760 °C for 16 h with an air quench process. Another sub-solvus heat treatment was conducted to the U720Li specimens, which covers a solution heat treatment at 1095 °C for 4 h followed by oil cooling and an aging heat treatment at 760 °C for 16 h with an air quench process.

The tensile tests were performed at both 25 °C and 750 °C by UTM5105, and the strain rate adopted in the test was 10^{-3} s^{-1}.

3. Results and Discussion

3.1. Composition Screening of Sc-Doped Superalloy

The microstructure of U720Li and RR1000 with different addition of scandium under different thermal consolidation processes are shown in Figure 2. The relative density of the specimens is shown in Figure 3 which is calculated by counting the area of pores through ImageJ software. As can be seen, the rise of thermal consolidation temperature can improve the relative density of the specimen, and the relative density can be improved to 99% basically with the temperature rising to 1150 °C, which means a higher temperature contributes to a denser microstructure within a certain range.

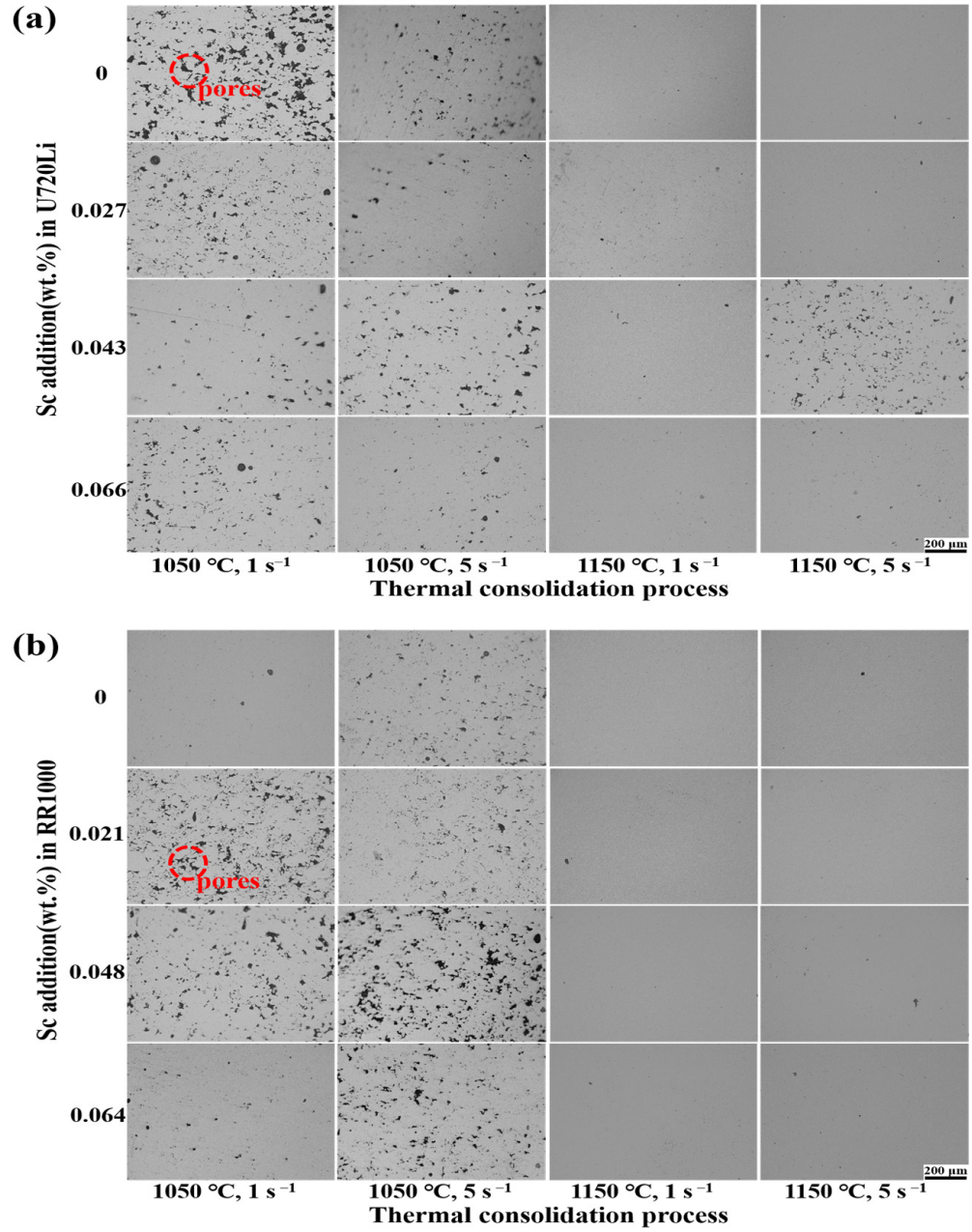

Figure 2. Metallograph of superalloys with different scandium addition under different thermal consolidation processes: (**a**) U720Li, (**b**) RR1000.

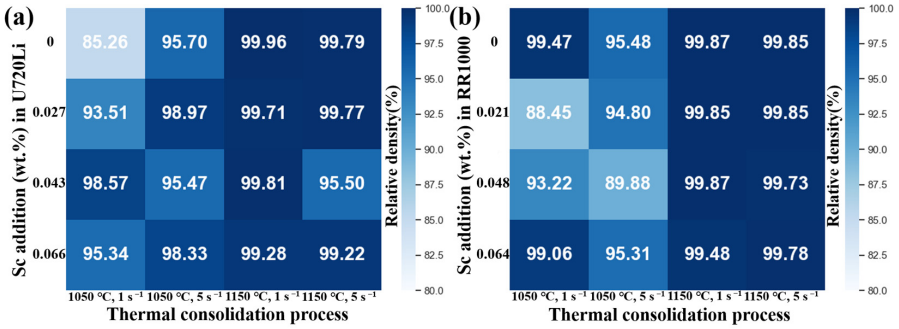

Figure 3. Relative density of superalloys with different scandium addition under different thermal consolidation processes: (**a**) U720Li, (**b**) RR1000.

The hardness of U720Li and RR1000 with different addition of scandium under different thermal consolidation processes are shown in Figure 4 and Table 3. It can be found that when the thermal consolidation temperature is 1150 °C, the hardness of the specimens is generally high, which can be attributed to the dense microstructure. Additionally, when adding 0.043 wt.% scandium, the hardness of U720Li reaches a peak of 386 HV3 at the temperature of 1050 °C and strain rate of 1 s^{-1}. In contrast, the hardness of U720Li decreases from 438 HV3 to 233 HV3 with scandium ranging from 0 wt.% to 0.043 wt.%, and increases to 534 HV3 with 0.066 wt.% scandium addition at the temperature of 1050 °C and strain rate of 5 s^{-1}. Similarly, the hardness of U720Li decreases from 512 HV3 to 472 HV3 with scandium ranging from 0 wt.% to 0.043 wt.%, and then increases to 485 HV3 with 0.066 wt.% scandium at the temperature of 1150 °C and strain rate of 1 s^{-1}. The hardness of U720Li prepared at the temperature of 1150 °C and strain rate of 5 s^{-1} remains a steady level of around 480 HV3. While in RR1000, the hardness decreases from 422 HV3 to 226 HV3 with scandium ranging from 0 wt.% to 0.048 wt.%, and then increases to 388 HV3 with 0.064 wt.% scandium. Compared with other Sc-doped superalloy, there is a relatively large deviation in RR1000 with 0.021 wt.% and 0.048 wt.% scandium under thermal consolidation parameter of 1050 °C and 1 s^{-1}, which may be ascribed to the fact that the alloy did not accomplish a dense microstructure at this condition. When further improving the temperature from 1050 °C to 1150 °C or strain rate from 1 s^{-1} to 5 s^{-1}, the hardness both reach the peak of 507 HV3 and 500 HV3 with 0.048 wt.% scandium addition. When simultaneously improving the temperature and strain rate, the hardness slightly decreases from 491 HV3 to 475 HV3 with scandium ranging from 0 wt.% to 0.048 wt.%, and increases to 531 HV3 with 0.064 wt.% scandium. As can be seen, 0.04 wt.%~0.05 wt.% scandium addition can be considered as an evident turning point in the Hardness-Sc addition curve. Therefore, superalloys with zero scandium addition, medium scandium addition (0.04 wt.%~0.05 wt.%) and high scandium addition (around 0.06 wt.%) are selected to further investigate the influence of scandium on the microstructure and mechanical properties through fast hot pressed sintering.

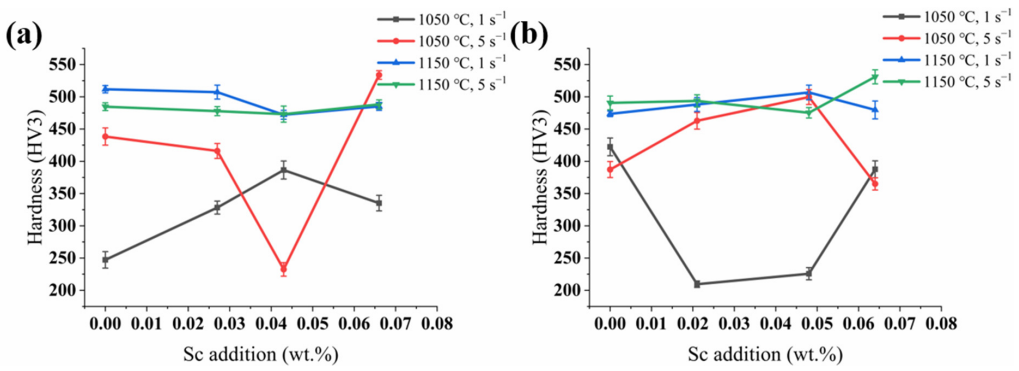

Figure 4. Hardness of superalloys with different scandium addition under different thermal consolidation processes: (**a**) U720Li, (**b**) RR1000.

Table 3. Hardness of superalloys with different scandium addition under different thermal consolidation processes (HV3).

Alloy	Scandium Addition (wt.%)	Thermal Consolidation Process (Temperature, Strain Rate)			
		1050 °C, 1 s^{-1}	1050 °C, 5 s^{-1}	1150 °C, 1 s^{-1}	1150 °C, 5 s^{-1}
U720Li	0	247 ± 13	438 ± 13	512 ± 6	485 ± 6
	0.027	328 ± 10	416 ± 12	507 ± 11	478 ± 7
	0.043	386 ± 14	233 ± 10	472 ± 7	473 ± 12
	0.066	335 ± 12	534 ± 7	485 ± 6	488 ± 7
RR1000	0	422 ± 14	387 ± 12	474 ± 4	491 ± 11
	0.021	210 ± 5	463 ± 13	488 ± 11	494 ± 9
	0.048	226 ± 9	500 ± 12	507 ± 11	475 ± 8
	0.064	388 ± 13	365 ± 9	480 ± 14	531 ± 11

3.2. The Existence of Scandium

Figure 5 shows the SEM image of Sc-doped RR1000 superalloy with relevant EDS analysis. It can be seen that there is a kind of white precipitate distributed in two RR1000 and an additional black phase in the RR1000-0.064. Then EDS surface scanning was carried out on the white precipitate and the black phase. The results illustrate that the white precipitate seems to be a kind of carbide combined with tantalum and titanium, while the black phase seems to be a kind of Sc-rich phase combined with oxygen. The carbide has a size of ~250 nm while the Sc-rich phase has a smaller size of ~200 nm. Similar results have been demonstrated by Deng et al. [10], in which definite peaks of scandium and oxygen are captured in the black phase through TEM and EDS analysis, indicating that scandium has the ability to react with oxygen in the Ni-based superalloy. In addition, due to the difference in the chemical composition, in which U720Li has no tantalum addition, the white carbides can hardly be observed.

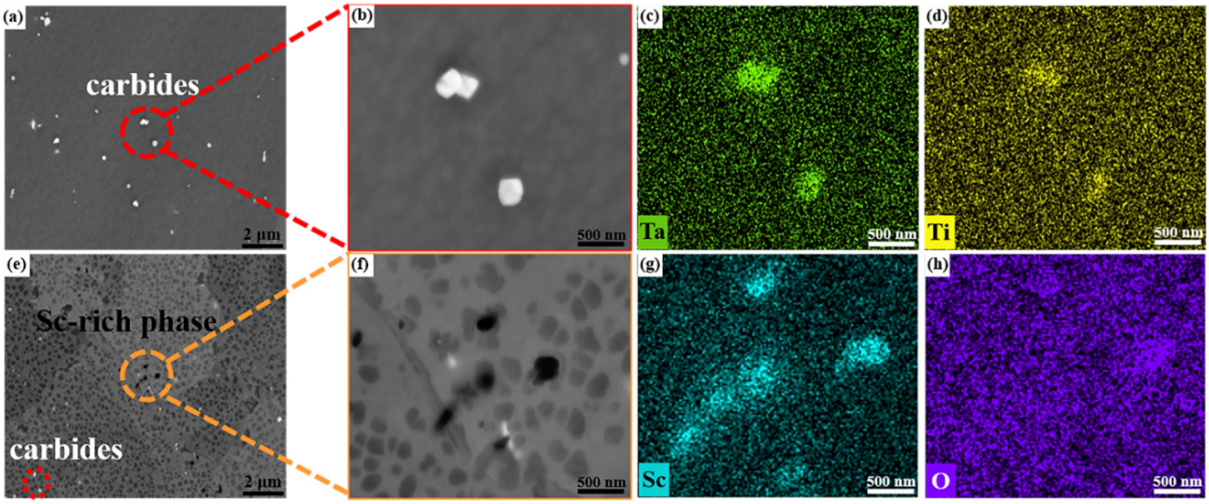

Figure 5. SEM image of Sc-doped RR1000 superalloy with relevant EDS analysis. (**a**,**b**) SE images of carbides in RR1000-0, (**c**,**d**) EDS analysis of carbides, (**e**,**f**) BSE images of Sc-rich phase in RR1000-0.064, (**g**,**h**) EDS analysis of Sc-rich phase.

3.3. Microstructure Evolution

Figure 6 depicts the morphology and distribution of gamma prime γ′ in U720Li with different scandium addition. As can be clearly seen, the distribution of γ′ in U720Li is typically tri-modal. Primary γ′ with the largest size (~600 nm) and irregular shape, precipitates unevenly at the grain boundary while secondary γ′ is uniformly dispersed within the grain with a medium size (~160 nm) and nearly spherical shape. Tertiary γ′ is distributed in the gap between primary γ′ and secondary γ′ with the smallest size (~30 nm).

Despite that the tri-modal distribution of γ′ exists in all three Sc-doped U720Li, the size and volume fraction of primary and secondary γ′ is different according to Table 4. It is apparent from Table 4 that there is an evident increase in the size of primary γ′ occurred from 552.9 nm to 662.1 nm with scandium addition increasing from 0 wt.% to 0.066 wt.%, along with the volume fraction of primary γ′ rising from 4.4% to 6.9%. Additionally, there is also an increase in the size and volume fraction of secondary γ′, especially the volume fraction of secondary γ′ rising to 30.5% when adding 0.043 wt.% scandium.

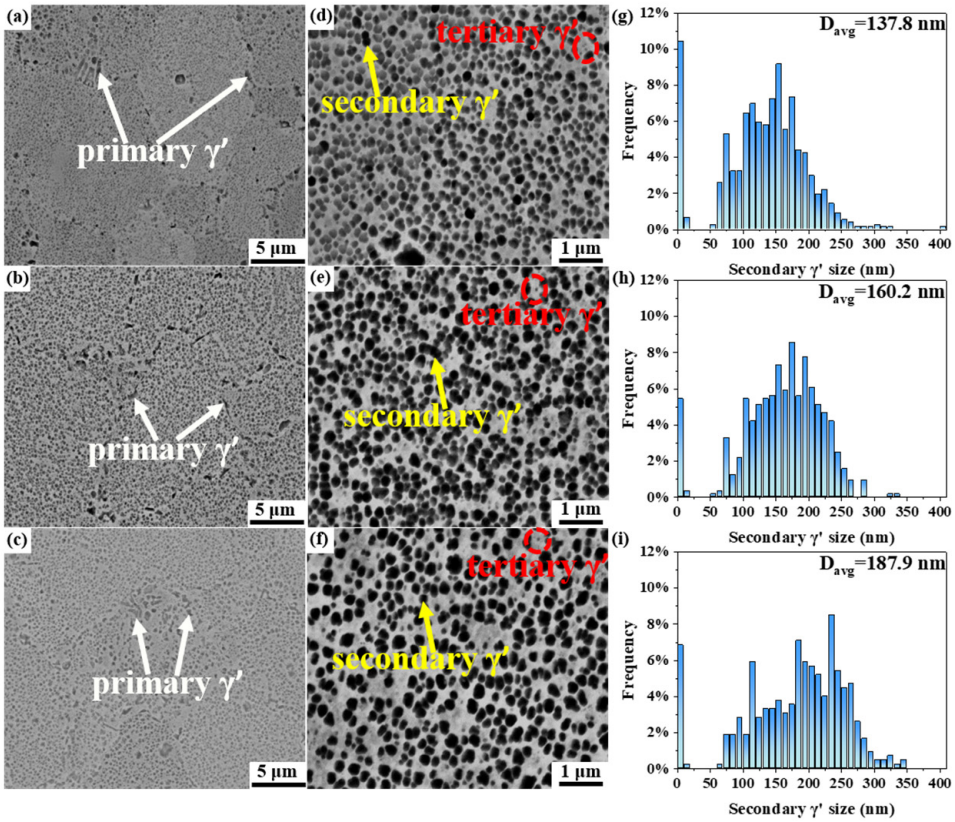

Figure 6. Morphology and distribution of γ′ in U720Li with different scandium addition. (**a**,**d**,**g**) 0 wt.% Sc, (**b**,**e**,**h**) 0.043 wt.% Sc, (**c**,**f**,**i**) 0.066 wt.% Sc.

Table 4. The size and volume fraction of primary and secondary γ′ in Sc-doped U720Li.

Alloy	Primary γ′		Secondary γ′	
	Average Diameter/nm	Volume Fraction/%	Average Diameter/nm	Volume Fraction/%
U-0	552.9	4.4	137.8	24.8
U-0.043	636.7	5.1	160.2	30.5
U-0.066	662.1	6.9	187.9	25.2

There are lots of similarities in the morphology and distribution of γ′ between RR1000 and U720Li. Firstly, tri-modal distribution of γ′ also appears in Sc-doped RR1000 according to Figure 7. Table 5 reveals an apparent rise in the size of primary γ′ as well as the volume fraction with increasing scandium addition. The size of secondary γ′ increases gradually while the volume fraction slightly decreases.

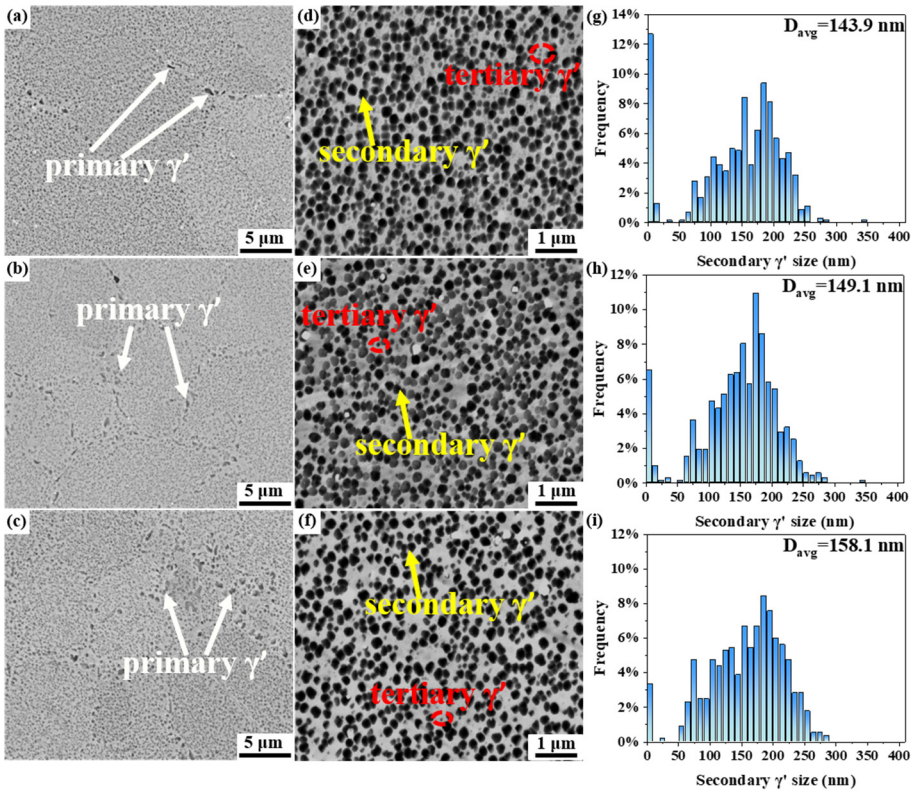

Figure 7. Morphology and distribution of γ′ in RR1000 with different scandium addition. (**a**,**d**,**g**) 0 wt.% Sc, (**b**,**e**,**h**) 0.048 wt.% Sc, (**c**,**f**,**i**) 0.064 wt.% Sc.

Table 5. The size and volume fraction of primary and secondary γ′ in Sc-doped RR1000.

Alloy	Primary γ′		Secondary γ′	
	Average Diameter/nm	Volume Fraction/%	Average Diameter/nm	Volume Fraction/%
R-0	544.1	1.1	143.9	26.1
R-0.048	629.8	5.1	149.1	25.9
R-0.064	675.2	6.3	158.1	24.4

From the results above, it can be found that scandium addition improves the growth and volume fraction of primary γ′ at the grain boundary and enlarges the size of secondary γ′. Previous study [29] has demonstrated that Sc in aluminum alloy prefers to bond with Al to form Al_3Sc. Al exists in the superalloy in the form of γ′-Ni_3Al, which shares a similar lattice structure with Al_3Sc, and it has been pointed out that Sc strongly prefers to substitute the Al site of γ′-Ni_3Al [30] in the superalloy. This may contribute to the precipitation of γ′ and hence improve the volume fraction of γ′ as the result of Sc enrichment in the γ′-Ni_3Al of superalloy. Meanwhile, Sc addition may change the lattice misfit between γ and γ′ and cause difference in the elastic energy and interfacial energy of γ′ [10], which may lead to the growth of γ′.

As exhibited in Figure 8, the distribution of γ′ in the U720Li remains tri-modal after heat treatment. However, some changes have taken place in the size and morphology of γ′. After a sub-solvus heat treatment, there is a sharp rise in the size of primary γ′ at the grain boundary. In addition, most primary γ′ in the U720Li with no scandium maintain a spherical shape while few primary γ′ is transformed into a cubic shape. Moreover, there is an increasing number of cubic-shape primary γ′ with the increasing scandium addition according to Figure 8b,c.

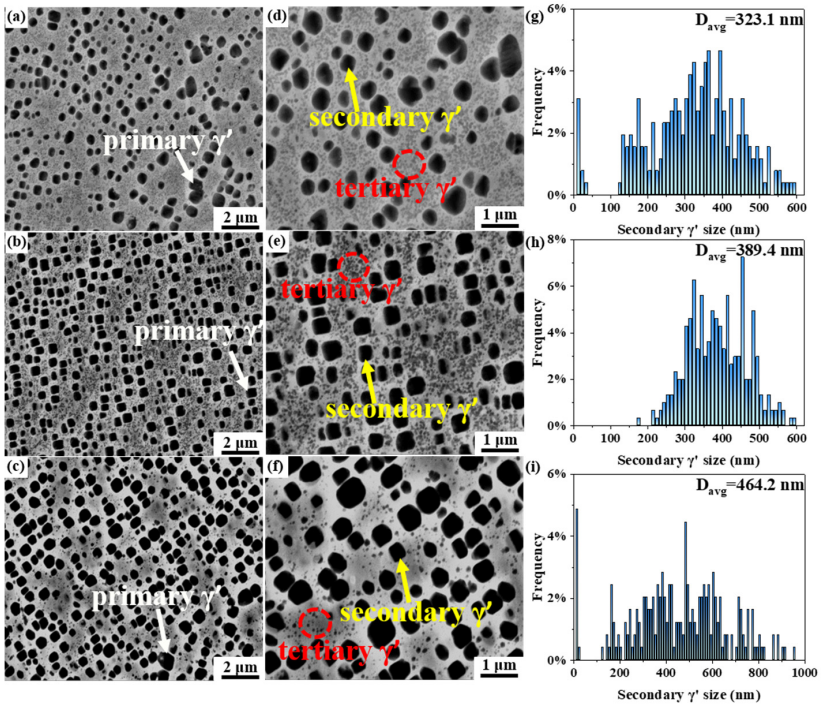

Figure 8. Morphology and distribution of γ′ in Sc-doped U720Li after heat treatment. (**a**,**d**,**g**) 0 wt.% Sc, (**b**,**e**,**h**) 0.043 wt.% Sc, (**c**,**f**,**i**) 0.066 wt.% Sc.

Some secondary γ′ with spherical shape still maintain the same size as a result of solution and instant precipitation during solution and aging heat treatment with oil quenching process. Besides, a fair proportion of secondary γ′ coarsen and grow up under high temperature, which results in the shape transformation from nearly spherical into cubic. Moreover, scandium seems to promote the transformation of the morphology of secondary γ′. The proportion of cubic secondary γ′ dramatically rises accompanied by the increase of average diameter of secondary γ′ according to Table 6.

Table 6. The size and volume fraction of secondary γ′ in Sc-doped U720Li after heat treatment.

Alloy	Average Diameter/nm	Volume Fraction/%
U-0	323.1	21.4
U-0.043	389.4	23.9
U-0.066	464.2	23.7

During heat treatment, the evolution of secondary γ′ usually goes through two periods, including diffusion-controlled coarsening regime and strain-induced shape transformation period [31]. Diffusion-controlled coarsening regime often occurs at the early stage of high temperature aging heat treatment, which can be described by classical LSW theory [32–34]. With secondary γ′ coarsening to the critical size, strain-induced shape transformation begins to play a leading role [32,35,36]. It has been reported that scandium addition can enhance the rate of diffusion-controlled coarsening and easily lead to strain-induced shape transformation by lowering the coarsening activation energy of secondary γ′. Furthermore, when shape transformation of secondary γ′ from spherical to cubic happens, it prefers to maintain the largest size with the increasing scandium addition [10]. The results in this work seems in good consistence with that.

Likewise, the size and morphology of γ′ in the RR1000 have changed a lot after heat treatment but still remain a tri-modal distribution. To begin with, the size of secondary γ′ declines generally compared with that of as-sintered specimens. Due to the different heat treatment process, secondary γ′ observed here, distinguished from the distinct growth of secondary γ′ in the U720Li, has an average size of 113 nm with nearly spherical shape

as can be seen from Figure 9 and Table 7. Meanwhile, with the increasing scandium addition, the size of secondary γ′ rises slightly accompanied by the gradual enlargement of volume fraction, which reveals that the addition of scandium still plays a role of coarsening. Moreover, the coarsening and shape transformation of primary γ′ seem more apparent, especially in the RR1000-0.064, where the primary γ′ has transformed into cubic with a larger size. This is corresponding with results observed in the U720Li, which illustrates that the addition of scandium facilitates the coarsening evolution of γ′.

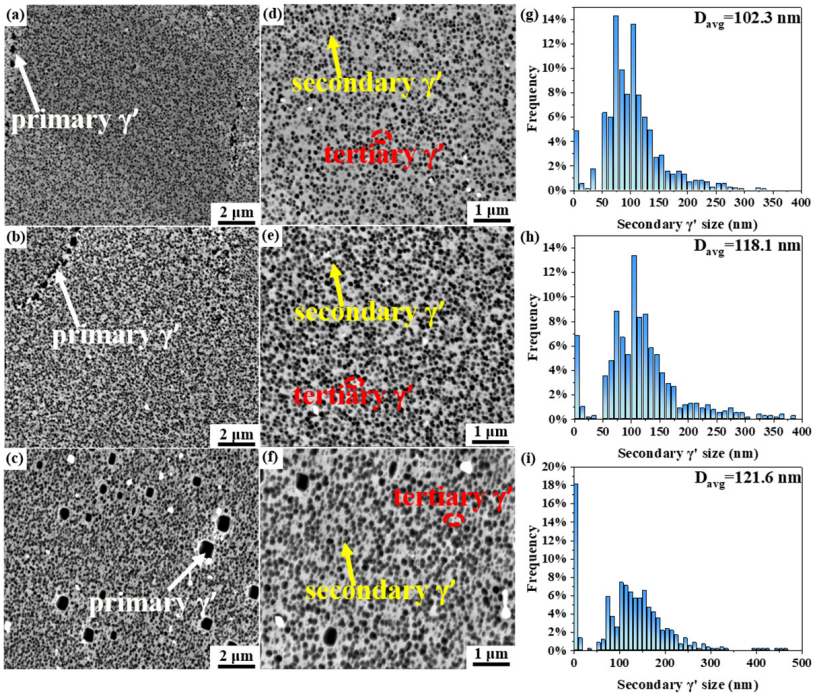

Figure 9. Morphology and distribution of γ′ in Sc-doped RR1000 after heat treatment. (**a**,**d**,**g**) 0 wt.% Sc, (**b**,**e**,**h**) 0.048 wt.% Sc, (**c**,**f**,**i**) 0.064 wt.% Sc.

Table 7. The size and volume fraction of secondary γ′ in Sc-doped RR1000 after heat treatment.

Alloy	Average Diameter/nm	Volume Fraction/%
R-0	102.3	20.8
R-0.048	118.1	26.1
R-0.064	121.6	28.8

As illustrated in Figures 10 and 11, the grain in Sc-doped U720Li is equiaxed in general. With the increase of scandium addition, the grain structure turns finer gradually, which is further demonstrated by frequency histogram of grain in Figure 10. As for as-sintered condition, the average grain size of U720Li with 0 wt.% Sc, 0.043 wt.% Sc and 0.066 wt.% Sc are 9.19 μm, 9.09 μm and 8.56 μm, respectively, which is calculated by Tango software. After heat treatment, the grain size hardly changes and the average grain size of U720Li with 0 wt.% Sc, 0.043 wt.% Sc and 0.066 wt.% Sc is 9.03 μm, 9.30μm and 10.88 μm, respectively, which can be ascribed to the primary γ′ located at the grain boundary. The primary γ′ plays a role of barrier in effectively hindering the grain boundary migration and hence refine the grain. Meanwhile the primary γ′ did not dissolve in the subsequent sub-solvus heat treatment [37], which can account for that the grain size after heat treatment remained essentially unchanged. It can be inferred that the grain refinement caused by scandium addition mainly happen in the sintering regime. In addition, the distribution of grain boundary misorientation displays that the high angle boundaries (HABS) play a dominant role. It can be seen that the ratio of HABS slightly increases in general after heat treatment, which may be related to recrystallization.

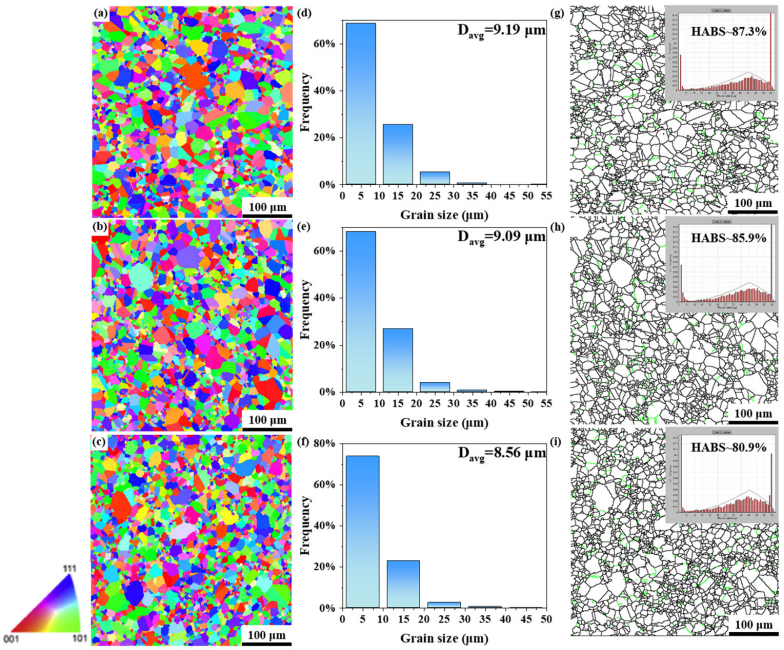

Figure 10. Inverse pole figure and Frequency histogram of grain together with distribution of grain boundary misorientation in as sintered Sc-doped U720Li: (**a**,**d**,**g**) 0 wt.% Sc, (**b**,**e**,**h**) 0.043 wt.% Sc, (**c**,**f**,**i**) 0.066 wt.% Sc. Green lines represent the low angle boundaries (LABs) (0–15°) but the high angle boundaries (HABs) (>15°) were indicated by black lines.

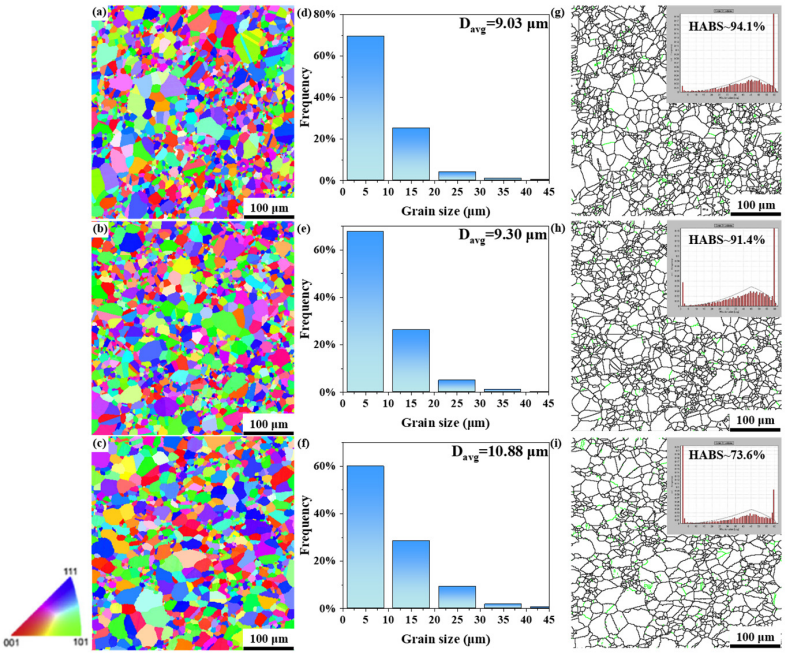

Figure 11. Inverse pole figure and Frequency histogram of grain together with distribution of grain boundary misorientation in heat-treated Sc-doped U720Li: (**a**,**d**,**g**) 0 wt.% Sc, (**b**,**e**,**h**) 0.043 wt.% Sc, (**c**,**f**,**i**) 0.066 wt.% Sc. Green lines represent the low angle boundaries (LABs) (0–15°) but the high angle boundaries (HABs) (>15°) were indicated by black lines.

Similarly, apparent equiaxed grain distribution and grain refinement can also be found in Sc-doped RR1000 according to Figures 12 and 13. As-sintered RR1000 with no scandium has the largest average grain size of 10.91 μm while the others with 0.048 wt.% and 0.064 wt.% scandium has a finer average grain size of 9.30 μm and 8.32 μm respectively, which confirms that scandium addition contributes to grain refinement. At the same

time, grain size after heat treatment is basically unchanged and still remains a decreasing trend along with increasing scandium content, which also verifies that grain refinement arising from scandium addition is accomplished during the sintering step. Additionally, the distribution of HABS in Sc-doped RR1000 superalloy is consistent with that of U720Li. And the dominant role of HABS seems more obvious after heat treatment.

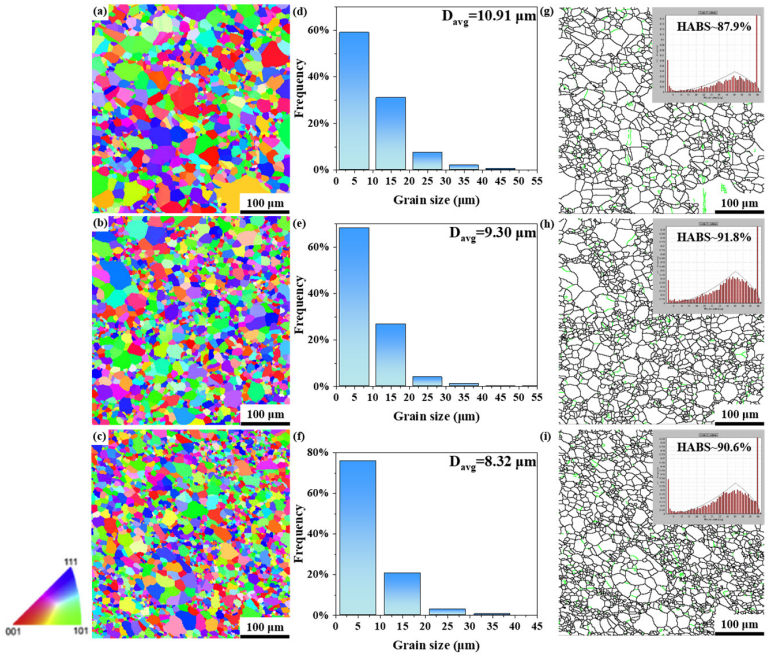

Figure 12. Inverse pole figure and Frequency histogram of grain together with distribution of grain boundary misorientation in as sintered Sc-doped RR1000: (**a**,**d**,**g**) 0 wt.% Sc, (**b**,**e**,**h**) 0.048 wt.% Sc, (**c**,**f**,**i**) 0.064 wt.% Sc. Green lines represent the low angle boundaries (LABs) (0–15°) but the high angle boundaries (HABs) (>15°) were indicated by black lines.

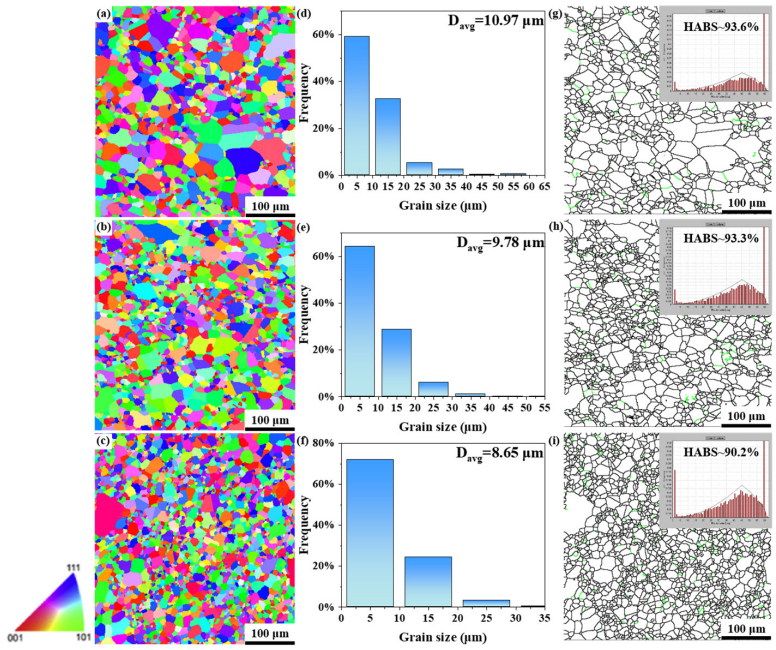

Figure 13. Inverse pole figure and Frequency histogram of grain together with distribution of grain boundary misorientation in heat-treated Sc-doped RR1000: (**a**,**d**,**g**) 0 wt.% Sc, (**b**,**e**,**h**) 0.048 wt.% Sc, (**c**,**f**,**i**) 0.064 wt.% Sc. Green lines represent the low angle boundaries (LABs) (0–15°) but the high angle boundaries (HABs) (>15°) were indicated by black lines.

Moreover, grain refinement can be put down to Zener pinning effect, which can be explained as the Equation (1) follows [37–40]:

$$P_z = K\gamma_{gb}\left(\frac{f}{r_p}\right) \quad (1)$$

where P_z is the Zener pinning pressure, K is a constant dependent on materials, γ_{gb} is the grain boundary energy, f represents the volume fraction of precipitates and r_p is the radius of precipitate.

In the Sc-doped superalloy above, K and γ_{gb} can be approximately deemed as constant for that only the content of scandium in the alloy changed slightly. Consequently, the Zener pinning pressure P_z can be determined based on the ratio of the volume fraction f and radius r_p of precipitate. The volume fraction and size of primary γ' in the Sc-doped superalloy have been proved to rise with the increasing scandium addition, and the increasing rate of volume fraction of primary γ' is a little higher than that of size of primary γ'. Therefore, the Zener pinning pressure P_z is gradually reinforced with the increasing scandium addition, and the superalloy with the highest scandium content has the finest average grain size generally.

3.4. Mechanical Properties

As shown in Figure 14, specimens prepared by fast hot pressed sintering achieve a high relative density of 99% in general, which was measured through Archimedes principle. And the hardness of as sintered Sc-doped superalloy both increase first and then slightly decrease with the increasing scandium content. Compared with as sintered condition, there is significant improvement in the hardness after heat treatment. Moreover, the hardness reaches the peak of 462 HV3 and 467 HV3 in U720Li and RR1000 when adding 0.06 wt.% scandium, which could be attributable to the impact of grain refinement.

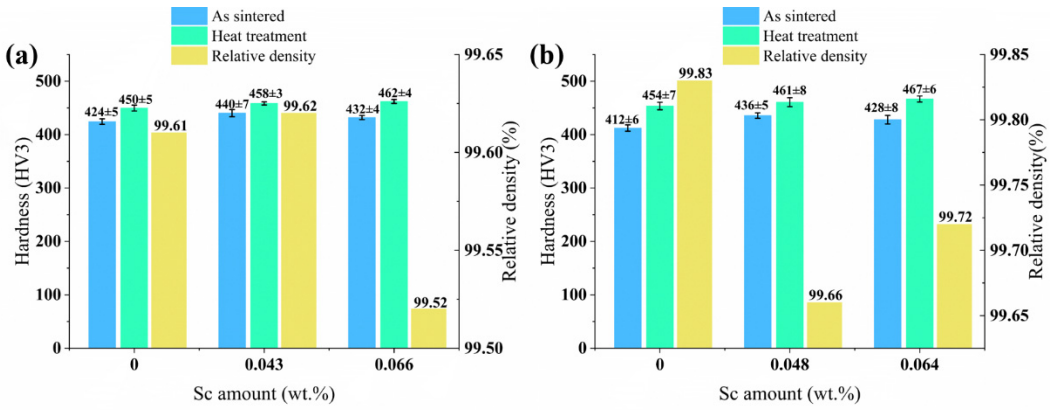

Figure 14. Hardness and relative density of Sc-doped superalloys under different conditions: (**a**) U720Li, (**b**) RR1000.

Tensile properties of Sc-doped U720Li at 25 °C and 750 °C under different conditions are displayed in Figure 15. For room temperature tensile properties, it can be clearly seen that the ultimate tensile strength (UTS) of both as-sintered and heat-treated U720Li with 0.043wt.% scandium reach a peak of 1561 MPa and 1520 MPa, respectively. Accordingly, the ductility of U720Li-0.043 under two conditions also reach the highest level of 32.5% and 15.25%, which represent the elongation to fracture. Besides, heat treatment is found to have an optimistic impact on the enhancement of yield strength (YS) of U720Li, and the YS of heat-treated U720Li-0.043 and U720Li-0.066 increases by 14.4% and 12.1% respectively compared with the as-sintered specimens.

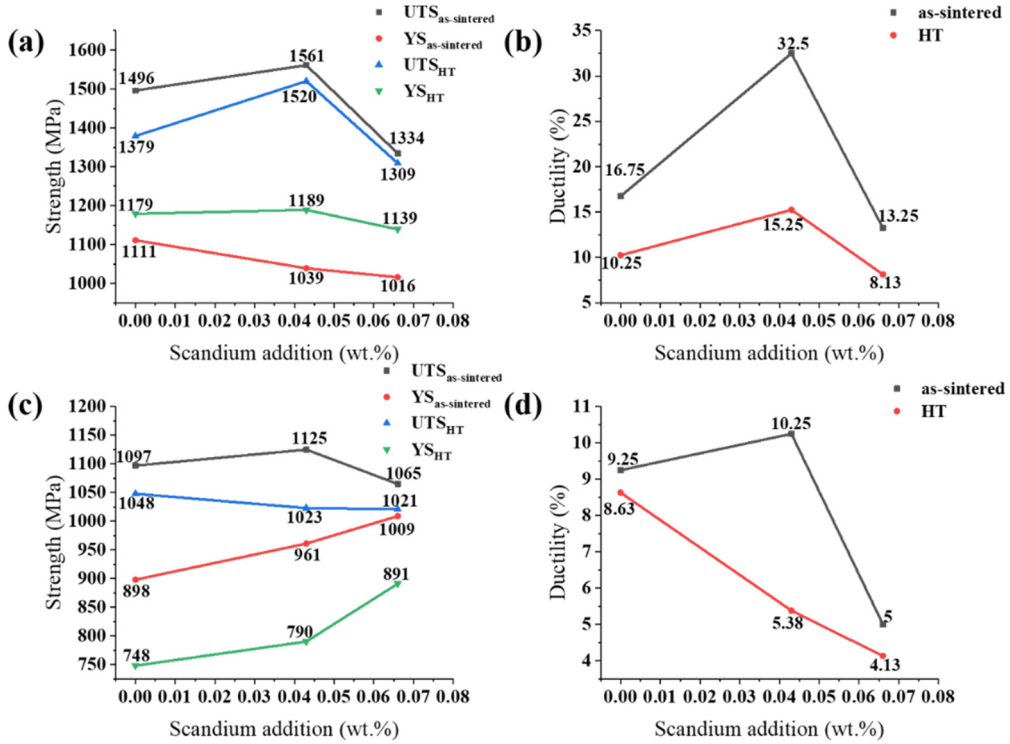

Figure 15. Tensile properties at 25 °C and 750 °C of Sc-doped U720Li under different conditions: (**a**,**b**) 25 °C, (**c**,**d**) 750 °C.

The as-sintered U720Li with 0.043 wt.% scandium still maintains a good combination of strength and ductility at 750 °C, of which the UTS, YS and ductility are 1125 MPa, 961 MPa and 10.25%, respectively. Moreover, Sc seems to play a significant role in improving the high temperature yield strength of the alloy; Compared with the alloy without Sc, when adding 0.066 wt.% Sc, the yield strength of as-sintered specimen increases from 898 MPa to 1009 MPa, increasing by 12.4%; After heat treatment, the yield strength of the sample increases from 748 MPa to 891 MPa, increasing by 19.1%.

The promotion of tensile properties in 0.043 wt.% Sc-doped U720Li may be ascribed to several aspects. To begin with, scandium addition contributes to the grain refinement and increases the density of grain boundary. Grain boundary can effectively impede the movement of dislocation and thereby enhance the strength and ductility. And Hall-Petch equation [41] can be used to further illuminate the grain boundary strengthening effect:

$$\sigma_{gb} = \sigma_0 + K_y / \sqrt{d} \quad (2)$$

where σ_{gb} represents the effect of grain boundary strengthening, σ_0 is a constant corresponding with material, K_y is the Hall-Petch constant, and d represents the average grain size. Despite that the grain refinement is not evident enough, it still plays a role in the good performance of U720Li-0.043 exhibited in the tensile test. As can be calculated from the Equation (2), U720Li-0.043 with a smaller grain size gets a higher improvement in grain boundary compared with U720Li without scandium. Furthermore, good combination of strength and elongation can be attributed to the size, volume fraction and distribution of γ' in the U720Li-0.043 as well. Compared with the two other U720Li alloy, γ' in the as-sintered U720Li-0.043 with a medium size has a larger volume fraction and homogeneous distribution. It has been reported that precipitate with fine size and uniform distribution is contributed to tensile properties in the Ni-based superalloy [6].

The enhancement of room temperature yield strength of heat-treated samples may be related to the evolution of size and morphology in γ' precipitate. As shown in Figure 8, γ' precipitate in the heat-treated sample begin to coarsen, and some γ' undergo the trans-

formation from spherical to cubic with scandium addition. Meanwhile, there are a large number of fine and dispersed tertiary γ′ in the heat-treated sample, especially in heat-treated U720Li-0 and U720Li-0.043.

It is generally accepted that there are two main interaction mechanisms between precipitates and dislocations during deformation, namely Orowan bypassing mode and shearing mode. And the stress required by shearing mode is generally higher than that of bypassing mode, which is corresponding with yield strength in the alloy. Whether the two mechanisms play a role in the alloy deformation depends on the size of the precipitate. It is reported that Orowan bypassing mode will play a dominant role during the deformation process when the γ′ precipitate surpasses a critical size (~400 nm) [42,43]. Therefore, the general improvement of room temperature yield strength of the heat-treated samples may be attributed to two aspects: First of all, there is more tiny tertiary γ′ dispersed in the heat-treated samples than as-sintered samples, and the shearing mode makes a greater contribution. The number of tertiary γ′ in the heat-treated U720Li-0 and U720Li-0.043 is also larger than that of the heat-treated U720Li-0.066. Accordingly, the yield strength is relatively higher in that more tertiary γ′ is sheared by dislocations; Besides, a small proportion of secondary γ′ in the heat-treated samples coarsen and exceed the critical size due to heat treatment and Sc addition, while others approach the critical size. And the size of γ′ precipitate with tri-modal distribution in the present work may exactly lie in a range, in which shearing mode could work together with Orowan bypassing mode during deformation [7,42,44,45], resulting in the overall improvement of yield strength in the heat-treated U720Li.

In the high temperature tensile test, the size and volume fraction advantage of γ′ precipitate in the as-sintered U720Li-0.043 account for its good performance. Additionally, high-temperature yield strength of as-sintered samples is generally better than that of heat-treated samples. Compared with the heat-treated U720Li, the γ′ precipitate in the as-sintered U720Li with an average size of 160 nm is distributed more evenly and orderly, and tends to have a narrower inter-particle space, which could force the γ matrix to deform together with precipitate and lead to a higher YS under high temperature [46]. In contrast, larger inter-particle space only enables the matrix to deform independently. Additionally, γ′ precipitate in the as-sintered U720Li is prone to pile up dislocations [46] at high temperature due to its size and volume fraction, which could enlarge the stress to shear precipitate and thereby contribute to the YS.

The results of high temperature tensile test also show that the yield strength of the as-sintered alloy enhances with the increase of Sc content. As mentioned before, the size of secondary γ′ increases gradually with the scandium addition without exceeding the critical size. Therefore, the shearing mode will play a leading role in high temperature deformation, and the shearing stress will rise with the size of precipitate within a range [47]. At the same time, secondary γ′ in the sample containing Sc with a relatively higher volume fraction may be easier to accumulate dislocations, which also enlarges the stress required for shearing.

Tensile properties of Sc-doped RR1000 at 25 °C and 750 °C under different conditions are displayed in Figure 16. It can also be found that the room temperature yield strength of heat-treated samples is significantly higher than that of as-sintered samples in general. The YS of RR1000-0 increases from 988 MPa to 1166 MPa, reaching an increasement of 18%; The YS of RR1000-0.048 increases from 977 MPa to 1161 MPa, reaching an increasement of 18.8%; The yield strength of RR1000-0.064 increases from 997 MPa to 1221 MPa, reaching an increasement of 22.5%. Despite that the tensile strength of the heat-treated samples has little change, the plasticity of the alloy has suffered certain damage. Therefore, as a reliable method to improve the yield strength, it is necessary to adjust heat treatment process to make a balance between the strength and plasticity.

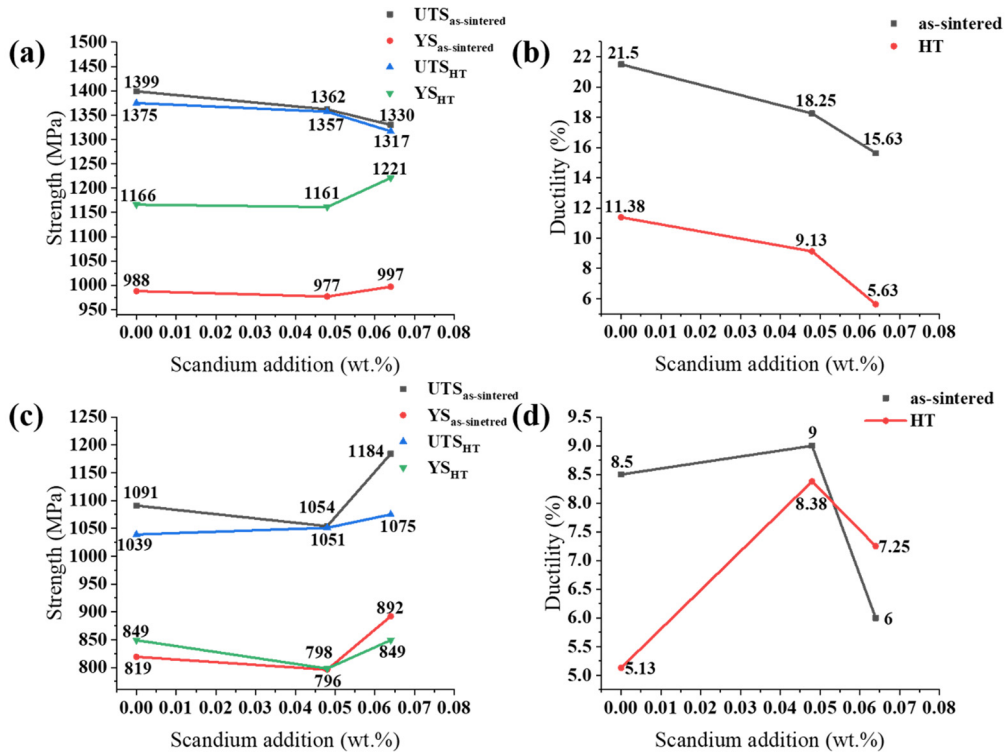

Figure 16. Tensile properties at 25 °C and 750 °C of Sc-doped RR1000 under different conditions: (**a**,**b**) 25 °C, (**c**,**d**) 750 °C.

The heat-treated RR1000 shares a similar γ′ distribution with as-sintered RR1000. Meanwhile, the average size of γ′ precipitate after heat treatment is 113 nm while that of as-sintered RR1000 is 150 nm. Both of them have chance to enable the γ matrix to deform together with precipitate while γ′ in the former has a smaller size and more compact distribution. The degree of γ and γ′ deformation in the heat-treated sample may be greater. In addition, the relatively higher volume fraction of γ′ precipitate after heat treatment would act as a greater obstacle for dislocations. Consequently, the enhancement range of YS after heat treatment is larger.

In the high temperature tensile test, as-sintered RR1000-0.064 has an excellent performance with a UTS of 1184 MPa, a YS of 892 MPa and a ductility of 6%, respectively. The potential reasons may lie in several aspects. First of all, the grain refinement introduced by scandium is noticeable in the RR1000. Accordingly, the grain boundary strengthening effect could make a big difference during the tensile test. In addition, scandium has a tendency to react with oxygen which has been discussed in Section 3.2. Consequently, it forms a tiny phase which is rich in scandium and dispersed in the alloy. For one thing, the consumption of oxygen can play a role of purification in the grain boundary and thereby reinforce the grain boundary, which can boost the strength and ductility of the alloy [16] For another, the dispersed tiny phase is also beneficial to the enhancement of tensile strength. Equally, the impact of dispersed distribution of γ′ precipitate cannot be neglected as well.

The fracture surface morphology of Sc-doped U720Li after room temperature and high temperature tensile test are exhibited in Figure 17. At room temperature tensile test, the fracture surface is mainly composed of dimples accompanied by fracture ridge, and a few of quasi-cleavage plane and intergranular fracture exist in certain specimens. Dimples are the typical symbol of ductile fracture, which demonstrates that the ductility of specimens at 25 °C is relatively good. In contrast, the quasi-cleavage plane and intergranular fracture seem to take the leading place in the fracture morphology at 750 °C. In addition, the poor ductility at 750 °C may be attributable to the defects in the superalloy. Analogously, the fracture surface morphology in Sc-doped RR1000 is similar with that in Sc-doped U720Li

according to Figure 18, which indicates the ductility at room temperature is good while at high temperature is poor.

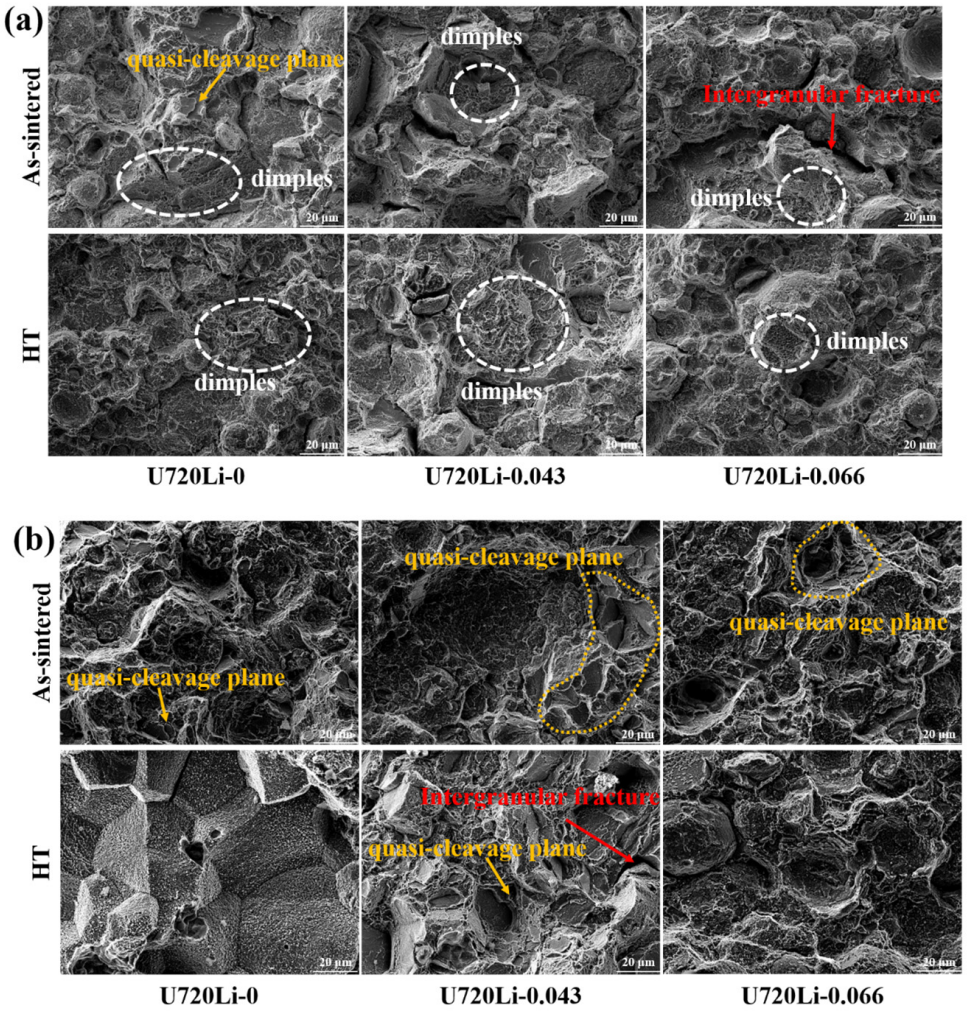

Figure 17. Fracture surface morphology of Sc-doped U720Li under different conditions: (**a**) 25 °C, (**b**) 750 °C.

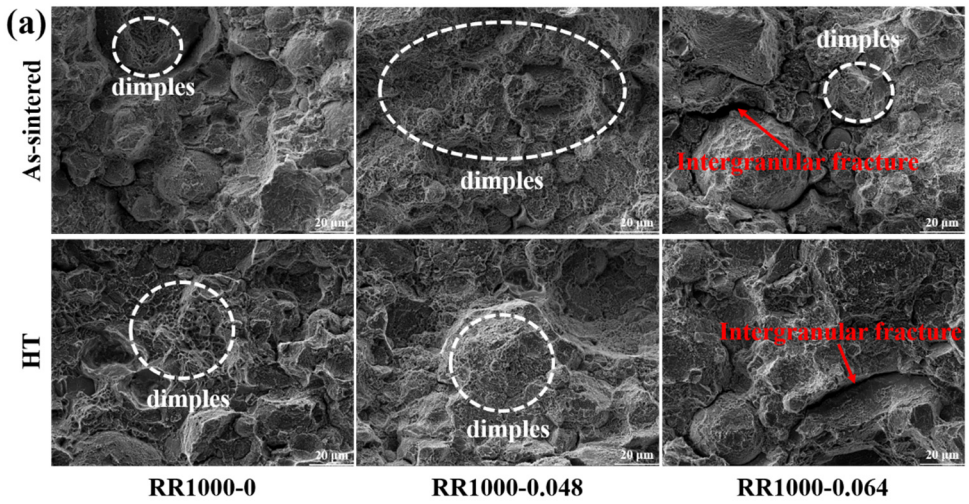

Figure 18. *Cont.*

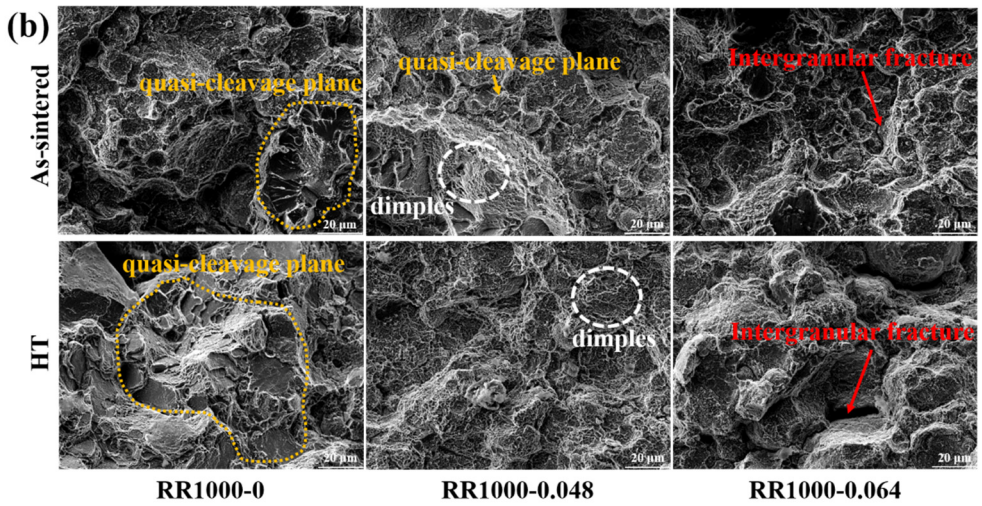

Figure 18. Fracture surface morphology of Sc-doped RR1000 under different conditions: (**a**) 25 °C, (**b**) 750 °C.

4. Conclusions

In this work, composition screening of two kinds of Sc-doped superalloy U720Li and RR1000 was accomplished through thermal consolidation process. Two groups of Sc-doped superalloy U720Li and RR1000 were fabricated through fast hot pressed sintering process to further investigate the effect of scandium on the microstructure and mechanical properties. The main conclusions can be drawn as follows:

(1) Scandium in the RR1000 will combine with oxygen and form oxides in the form of a tiny phase distributed in the matrix.

(2) The addition of scandium can effectively refine the grain size through enlarging the size and volume fraction of primary γ′ precipitate distributed at the grain boundary.

(3) Scandium addition has contributed to the growth and precipitation of secondary γ′ to some extent. Especially in the Sc-doped U720Li superalloy after heat treatment, the coarsening effect of scandium is fairly apparent, which enhance the coarsening rate of secondary γ′ and promote the shape transformation from spherical into cubic during the heat treatment process.

(4) Grain refinement arising from scandium boost the hardness of specimens, especially after heat treatment. The as-sintered U720Li with 0.043 wt.% scandium and RR1000 with 0.064 wt.% scandium both have excellent mechanical properties at ambient and elevated temperature, which could be attributed to the comprehensive effects of γ′ precipitate modification and grain boundary strengthening.

(5) It is necessary to adjust heat treatment to enhance the yield strength of Sc-doped superalloy as well as make a balance between the strength and plasticity.

Author Contributions: Writing—original draft, Conceptualization, Investigation, L.Y.; Writing—review & editing, Supervision, F.L. Data analysis, Investigation, H.D.; Investigation, X.O. Investigation, X.X. Resources, Language polishing and Supervision, L.T.; Resources, Supervision, L.H. All authors have read and agreed to the published version of the manuscript.

Funding: This research was financially supported by National Science and Technology Major Project (J2019-IV-0003-0070), the Natural Science Foundation of China (91860105, 52074366), Natural Science Foundation of Hunan Province of China (2021JJ40757), the Science and Technology Innovation Program of Hunan Province (2021RC3131), and Project Supported by State Key Laboratory of Powder Metallurgy, Central South University, Changsha, China.

Data Availability Statement: The data presented in this study are available within the article.

Conflicts of Interest: The authors declare that they have no conflict of interest.

References

1. Liu, F.; Wang, Z.-X.; Wang, Z.; Zhong, J.; Zhao, L.; Jiang, L.; Zhou, R.-H.; Liu, Y.; Huang, L.; Tan, L.-M.; et al. High-Throughput Method–Accelerated Design of Ni-Based Superalloys. *Adv. Funct. Mater.* **2022**, *32*, 2109367. [CrossRef]
2. Qin, Z.-J.; Wang, Z.; Wang, Y.-Q.; Zhang, L.-N.; Li, W.-F.; Liu, J.; Wang, Z.-X.; Li, Z.-H.; Pan, J.; Zhao, L.; et al. Phase prediction of Ni-base superalloys via high-throughput experiments and machine learning. *Mater. Res. Lett.* **2021**, *9*, 32. [CrossRef]
3. Gayda, J.; Gabb, T.P.; Kantzos, P.T. The Effect of Dual Microstructure Heat Treatment on an Advanced Nickel-Base Disk Alloy. In Proceedings of the International Symposium on Superalloys, Cleveland, OH, USA, 19–23 September 2004; p. 323. [CrossRef]
4. Zhu, C.Z.; Zhang, R.; Cui, C.Y.; Zhou, Y.Z.; Liang, F.G.; Liu, X.; Sun, X.F. Influence of Ta content on microstructure and creep behavior of a Ni–Co base disc superalloy. *Mater. Sci. Eng. A* **2021**, *802*, 140646. [CrossRef]
5. Zhang, G.Q.; Zhang, Y.W.; Zheng, L.; Peng, Z.C. Research Progress in Powder Metallurgy Superalloys and Manufacturing Technologies for Aero-Engine Application. *Acta Metall. Sin.* **2019**, *55*, 1133. [CrossRef]
6. Preuss, M.; Fonseca, J.; Grant, B.; Knoche, E.; Moat, R.J.; Daymond, M. The Effect of γ′ Particle Size on the Deformation Mechanism in an Advanced Polycrystalline Nickel-Base Superalloy. In Proceedings of the International Symposium on Superalloys 2008, Champion, PA, USA, 14–18 September 2008; p. 405. [CrossRef]
7. Kozar, R.W.; Suzuki, A.; Milligan, W.W.; Schirra, J.J.; Savage, M.F.; Pollock, T.M. Strengthening Mechanisms in Polycrystalline Multimodal Nickel-Base Superalloys. *Metall. Mater. Trans. A* **2009**, *40*, 1588. [CrossRef]
8. Thébaud, L.; Villechaise, P.; Crozet, C.; Devaux, A.; Béchet, D.; Franchet, J.-M.; Rouffié, A.-L.; Mills, M.; Cormier, J. Is there an optimal grain size for creep resistance in Ni-based disk superalloys? *Mater. Sci. Eng. A* **2018**, *716*, 274–283. [CrossRef]
9. Xu, K.-D.; Ren, Z.-M.; Li, C.-J. Progress in application of rare metals in superalloys. *Rare Met.* **2014**, *33*, 111. [CrossRef]
10. Deng, R.; Liu, F.; Tan, L.-M.; Zhang, S.-Y.; Liu, Y.; Huang, L. Effects of scandium on microstructure and mechanical properties of RR1000. *J. Alloys Compd.* **2019**, *785*, 634. [CrossRef]
11. Pan, X.L.; Yu, H.Y.; Tu, G.F.; Sun, W.R.; Hu, Z.Q. Effect of rare earth metals on solidification behaviour in nickel based superalloy. *Mater. Sci. Technol.A* **2012**, *28*, 560. [CrossRef]
12. Kang, D.S.; Koizumi, Y.; Yamanaka, K.; Aoyagi, K.; Bian, H.-K.; Chiba, A. Significant impact of yttrium microaddition on high temperature tensile properties of Inconel 713C superalloy. *Mater. Lett.* **2018**, *227*, 40. [CrossRef]
13. Li, X.L.; He, S.M.; Zhou, X.T.; Zou, Y.; Li, Z.J.; Li, A.G.; Yu, X.H. Effects of rare earth yttrium on microstructure and properties of Ni–16Mo–7Cr–4Fe nickel-based superalloy. *Mater. Charact.* **2014**, *95*, 171. [CrossRef]
14. Zhou, P.J.; Yu, J.J.; Sun, X.F.; Guan, H.R.; He, X.M.; Hu, Z.Q. Influence of Y on stress rupture property of a Ni-based superalloy. *Mater. Sci. Eng. A* **2012**, *551*, 236. [CrossRef]
15. Song, X.; Wang, L.; Liu, Y.; Ma, H.-P. Effects of temperature and rare earth content on oxidation resistance of Ni-based superalloy. *Prog. Nat. Sci. Mater. Int.* **2011**, *21*, 227. [CrossRef]
16. Bian, W.-D.; Zhang, H.-R.; Zhang, X.-L.; Gao, M.; Li, J.-P.; Li, Q.-L.; Cui, Y.-S.; Zhang, H. Comprehensive influence of Y on K417 superalloy: Purification, interactions among the alloy elements and high temperature properties. *Mater. Sci. Eng. A* **2019**, *755*, 190. [CrossRef]
17. Guimarães, A.V.; R, M.S.D.S.; Almeida, L.H.D.; Araujo, L.S.; Farina, A.B.; François Dille, J.A. Influence of yttrium addition on the microstructural evolution and mechanical properties of superalloy 718. *Mater. Sci. Eng. A* **2020**, *776*, 139023. [CrossRef]
18. Banoth, S.; Palleda, T.N.; Shimazu, S.; Kakehi, K. Yttrium's Effect on the Hot Cracking and Creep Properties of a Ni-Based Superalloy Built Up by Additive Manufacturing. *Materials* **2021**, *14*, 1143. [CrossRef]
19. Cao, S.-T.; Yang, Y.-Q.; Chen, B.; Liu, K.; Ma, Y.-C.; Ding, L.-L.; Shi, J.-J. Influence of yttrium on purification and carbide precipitation of superalloy K4169. *J. Mater. Sci. Technol.* **2021**, *86*, 260. [CrossRef]
20. Song, X.; Wang, L.; Liu, Y.; Ma, H.-P. Study on the Mechanical Performance of a Ni-Based Superalloy with Trace Rare Earth Element La Additions. *Adv. Mater. Res.* **2012**, *509*, 177. [CrossRef]
21. Luis, E.G.A.; Bedolla-Jacuinde, A.; Guerra, F.V.; Ruiz, A. Influence of Rare Earth Additions to an Inconel 718 Alloy. *MRS Adv.* **2020**, *5*, 3035. [CrossRef]
22. Song, X.; Wang, L.; Liu, Y.; Ma, H.-P. Precipitation characteristics and La effects on precipitates of a new 22Cr-14W-2Mo superalloy. *Rare Met.* **2010**, *29*, 132. [CrossRef]
23. Cui, C.-Y.; Han, G.-M.; Sun, X.-F. Effect of Ce Addition on the Microstructures and Mechanical Properties of a Ni-Co-Based Superalloy. *Adv. Mater. Res.* **2012**, *415*, 2062–2065. [CrossRef]
24. Liu, L.-F.; Wu, S.-S.; Chen, Y.; LÜ, S.-L. Oxidation behavior of RE-modified nickel-based superalloy between 950 °C and 1150 °C in air. *Trans. Nonferrous Met. Soc. China* **2016**, *26*, 1163. [CrossRef]
25. Rehman, K.; Sheng, N.-C.; Sang, Z.-R.; Xun, S.-L.; Wang, Z.-J.; Xie, J.; Hou, G.-C.; Zhou, Y.-Z.; Sun, X.-F. Comparative study of the reactive elements effects on oxidation behavior of a Ni-based superalloy. *Vacuum* **2021**, *191*, 110382. [CrossRef]
26. Bai, J.-Y.; Wu, J.-H.; Xu, S.-H.; Pei, Y.-L.; Qin, L.; Li, S.-S.; Gong, S.-K. Effects of Ce and Dy on the Cyclic Oxidation Behavior of a Ni-Based Single Crystal Superalloy. In *Proceedings of the High Performance Structural Materials*; Springer: Singapore, 2018; Volume 803, pp. 803–814. [CrossRef]
27. Wei, B.; Liu, Z.-M.; Cao, B.; Nong, B.-Z.; Zhang, Y.-Z.; Zhou, H.; Ai, Y.-K. Selective laser melting of crack-free René 104 superalloy by Sc microalloying. *J. Alloys Compd.* **2022**, *895*, 162663. [CrossRef]
28. Wei, B.; Cao, B.; Liu, Z.-M.; Zhou, H.; Nong, B.-Z.; Zhang, Y.-Z. Additive manufacturing of Sc microalloyed René 104 superalloy: Powder properties and cracking elimination. *Adv. Powder Technol.* **2022**, *33*, 103430. [CrossRef]

29. Kendig, K.L.; Miracle, D.B. Strengthening mechanisms of an Al-Mg-Sc-Zr alloy. *Acta Mater.* **2002**, *50*, 4165. [CrossRef]
30. Wen, M.-R.; Wang, C.-Y. Transition-metal alloying of γ′-Ni3Al: Effects on the ideal uniaxial compressive strength from first-principles calculations. *Phys. Rev. B* **2018**, *97*, 024101. [CrossRef]
31. Chen, Y.-Q.; Prasath babu, R.; Slater, T.J.A.; Bai, M.-W.; Mitchell, R.; Ciuca, O.; Preuss, M.; Haigh, S.J. An investigation of diffusion-mediated cyclic coarsening and reversal coarsening in an advanced Ni-based superalloy. *Acta Mater.* **2016**, *110*, 295. [CrossRef]
32. Doi, M. Coarsening Behaviour of Coherent Precipitates in Elastically Constrained Systems & mdash;With Particular Emphasis on Gamma-Prime Precipitates in Nickel-Base Alloys & mdash. *Mater. Trans. JIM* **1992**, *33*, 637. [CrossRef]
33. Lifshitz, I.M.; Slyozov, V.V. The kinetics of precipitation from supersaturated solid solutions. *J. Phys. Chem. Solids* **1961**, *19*, 35. [CrossRef]
34. Chellman, D.J.; Ardell, A.J. The coarsening of γ′ precipitates at large volume fractions. *Acta Metall.* **1974**, *22*, 577. [CrossRef]
35. Khachaturyan, A.G.; Semenovskaya, S.V.; Morris, J.W. Theoretical analysis of strain-induced shape changes in cubic precipitates during coarsening. *Acta Metall.* **1988**, *36*, 1563. [CrossRef]
36. Doi, M.; Miyazaki, T.; Wakatsuki, T. The effect of elastic interaction energy on the morphology of γ′precipitates in nickel-based alloys. *Mater. Sci. Eng.* **1984**, *67*, 247. [CrossRef]
37. Collins, D.M.; Conduit, B.D.; Stone, H.J.; Hardy, M.C.; Conduit, G.J.; Mitchell, R.J. Grain growth behaviour during near-γ′ solvus thermal exposures in a polycrystalline nickel-base superalloy. *Acta Mater.* **2013**, *61*, 3378. [CrossRef]
38. Smith, C.S. Introduction to Grains, Phases, and Interfaces—An Interpretation of Microstructure. *Trans. AIME* **1948**, *175*, 15.
39. Song, K.; Aindow, M. Grain growth and particle pinning in a model Ni-based superalloy. *Mater. Sci. Eng. A* **2008**, *479*, 365. [CrossRef]
40. Manohar, P.A.; Ferry, M.; Chandra, T. Five Decades of the Zener Equation. *ISIJ Int.* **1998**, *38*, 913. [CrossRef]
41. Hall, E.O. The Deformation and Ageing of Mild Steel: III Discussion of Results. *Proc. Phys. Soc. B* **1951**, *64*, 747. [CrossRef]
42. Grant, B.M.B.; Francis, E.M.; Quinta da Fonseca, J.; Daymond, M.R.; Preuss, M. Deformation behaviour of an advanced nickel-based superalloy studied by neutron diffraction and electron microscopy. *Acta Mater.* **2012**, *60*, 6829. [CrossRef]
43. Xia, P.C.; Yu, J.J.; Sun, X.F.; Guan, H.R.; Hu, Z.Q. Influence of thermal exposure on γ′ precipitation and tensile properties of DZ951 alloy. *Mater. Charact.* **2007**, *58*, 645. [CrossRef]
44. Heilmaier, M.; Leetz, U.; Reppich, B. Order strengthening in the cast nickel-based superalloy IN 100 at room temperature. *Mater. Sci. Eng. A* **2001**, *375*, 319–321. [CrossRef]
45. Zhang, P.; Yuan, Y.; Li, B.; Guo, S.W.; Yang, G.X.; Song, X.L. Tensile deformation behavior of a new Ni-base superalloy at room temperature. *Mater. Sci. Eng. A* **2016**, *655*, 152. [CrossRef]
46. Francis, E.M.; Grant, B.M.B.; Fonseca, J.Q.; Phillips, P.J.; Mills, M.J.; Daymond, M.R.; Preuss, M. High-temperature deformation mechanisms in a polycrystalline nickel-base superalloy studied by neutron diffraction and electron microscopy. *Acta Mater.* **2014**, *74*, 18. [CrossRef]
47. Sharghi-Moshtaghin, R.; Asgari, S. The influence of thermal exposure on the γ′ precipitates characteristics and tensile behavior of superalloy IN-738LC. *J. Mater. Process. Technol.* **2004**, *147*, 343. [CrossRef]